

Research Article

Analysis and Modeling of Particle Velocities in Premixed Abrasive Water Jets

Wei qin Zuo ^{1,2}, Cheng Huang,^{1,2} Yanwei Liu,^{1,2} Hongkai Han ^{1,2}, Fuchang Hao,^{1,2}
Fajun Zhao,^{1,2} and Fei Huang³

¹State Key Laboratory Cultivation Base for Gas Geology and Gas Control, Henan Polytechnic University, Jiaozuo, 454000 Henan Province, China

²School of Safety Science and Engineering, Henan Polytechnic University, Jiaozuo, 454000 Henan Province, China

³School of Resources & Environment and Safety Engineering, Hunan University of Science and Technology, Xiangtan, 411100 Hunan Province, China

Correspondence should be addressed to Hongkai Han; hkh@hpu.edu.cn

Received 22 July 2020; Revised 18 September 2020; Accepted 3 October 2020; Published 25 October 2020

Academic Editor: Guozhong Hu

Copyright © 2020 Wei qin Zuo et al. This is an open access article distributed under the Creative Commons Attribution License, which permits unrestricted use, distribution, and reproduction in any medium, provided the original work is properly cited.

The premixed abrasive jet possesses a strong strike ability and is widely used in oil and gas exploitation, machining, rust removal, and other fields. The superstrong, forceful impact of the premixed abrasive jet is mainly provided by high-speed abrasive groups. Hence, the abrasive velocity is the basis of this research, by applying the distribution law of abrasive impact force. In this paper, the particle velocity of the premixed abrasive jet is analyzed theoretically, and the corresponding particle velocity model is established. The real-time contrast interpolation method is employed to solve the problem of the variable drag coefficient. Factors such as the nozzle structure, average abrasive diameter, abrasive density, and jet flow are utilized to determine the abrasive velocity of the nozzle outlet. The numerical solution for the abrasive velocity is obtained by dividing the high-pressure pipe and nozzle into several sections, along the axis. Finally, the calculated particle velocity is compared with the particle image velocity measurement (PIV), to verify the correctness of the established model. These results demonstrate that the model calculation is in effective agreement with the experimental results. The deviation between the theoretical value and the experimental mean is 0.18 m/s. The standard deviation of the experimental results is 3.81–4.22 m/s, while the average error is less than 4%.

1. Introduction

Abrasive water jet technology has seen rapid development in modern times. It is widely used in industrial cutting, tunneling, surface cleaning, and drilling applications [1–3] due to characteristics that include cold state, spot cutting, universality, good cutting quality, and strong cutting performance; this technology is also environmentally protective and pollution-free. It is well known that the striking force of the premixed abrasive jet is provided primarily by the abrasive itself and that the striking force is closely related to the speed of the abrasive. The velocity field of the premixed abrasive jet is studied to provide support for the analysis of the distribution law in abrasive jet hitting force; based on this work, the

acceleration process and acceleration mechanism of the abrasive jet are analyzed in-depth.

There are complex pulsation mechanisms in an abrasive water jet, which are affected by various forces in the process of acceleration. Research on abrasive jets has previously focused on experimental means and numerical abrasive assessments; however, this theoretical research does not provide a thorough understanding of these mechanisms. Hlaváč et al. [4, 5] and Liu et al. [6] conducted stress analysis on a single abrasive and then established a motion equation for the abrasive; although these results were useful, the stress analysis of the abrasive jet in the flow field was not comprehensive. Chen and Siores [7], Haj Mohammad Jafar et al. [8], Laniel et al. [9], Wang et al. [10], and Liu et al. [11]

studied the abrasive jet flow field by using the numerical simulation method and achieved good results. However, due to the complex pulsation phenomenon of the abrasive jet, the results obtained from numerical simulation were still far from the actual flow field of the abrasive jet. Stevenson and Hutchings [12] and Huang et al. [13, 14] conducted research on abrasive jets using experimental methods and reached some beneficial conclusions. Swanson et al. [15] and Miller and Archibald [16] used two electromagnetic induction coils to measure the movement process of abrasive particles in a postmixing collimator. This method was limited in that it could only measure the average velocity of abrasive particles in a certain section and failed to obtain the radial position of abrasive particles in the jet. Momber and Kovacevic [17] calculated the time integral of the jet impact force according to the impact momentum relationship and obtained the relationship between jet velocity and jet impact force. This method was simple to execute but was only capable of measuring jet velocity after the jet penetrated the workpiece. However, these previous studies mostly treated the drag coefficient, a key parameter, as a constant and did not consider the influence of the Basset force on the abrasive acceleration; thus, it was difficult to comprehensively analyze the problem of abrasive stress.

In recent years, domestic and foreign scholars have conducted in-depth research on various flow fields by using PIV technology (particle image velocimeter) and, in doing so, have achieved productive results [18]. This technology provides for a type of noncontact measurement with large testing ranges and high precisions, which is widely used in various flow field tests. The measurement principle is as follows: under the premise of reasonably assigning pulse time, the flow field illuminated by the pulse-type laser plate light source is captured by a camera, and a series of images of the flow field tracer particles are obtained. The images are analyzed for correlation, and the velocity of the flow field is represented by the displacement of the tracer particles. To ensure a high correlation coefficient for correlation analysis, it is necessary to ensure that each image query interval has 5-10 tracer particles. For ordinary liquid flow field, trace particles at specific concentrations can be added to the fluid. For an abrasive jet, tracer particles cannot represent abrasive displacement, and since abrasive particles are large in size, it is difficult to reach a concentration of 5-10 particles within each query interval. Therefore, it remains difficult to test the abrasive velocity field directly with PIV technology alone. To this end, this paper proposes using PIV technology in combination with an independent abrasive center recognition program, thus realizing a noncontact testing method and using real-time comparison interpolation analysis. The influence of the resistance coefficient and the Basset force on abrasive acceleration can then be assessed, and an abrasive movement differential equation can be developed, which is solved by an iterative algorithm to achieve a more comprehensive and accurate interpretation of the abrasive mechanism of acceleration.

2. Abrasive Force Analysis

The abrasive is subjected to the following main forces during acceleration: viscous resistance, virtual mass, Basset force, pres-

sure gradient force, Magnus force, and Saffman force. According to Newton's second law of motion, the Euler form of the differential equation for abrasive motion can be expressed as

$$\begin{aligned} \frac{4\pi}{3} r_p^3 \rho_p \frac{dV_p}{dt} = & C_D \frac{1}{2} \rho_f |V_f - V_p| (V_f - V_p) S \\ & + \frac{2}{3} \pi \cdot r_p^3 \rho_f \frac{d}{dt} (V_f - V_p) \\ & + 6r_p^2 \sqrt{\pi \mu \rho_f} \int_{t_{p0}}^{t_p} \frac{1}{\sqrt{t_p - \tau}} \left(\frac{d}{dt} (V_f - V_p) \right) \\ & \cdot d\tau - \left(\frac{4}{3} \pi r_p^3 \right) \frac{\partial p}{\partial x} + F_{ML} + F_S, \end{aligned} \quad (1)$$

where r_p is the abrasive radius, subscript f is the liquid phase, subscript p is the abrasive, ρ is the density, V is the velocity, t is the time, C_D is the drag coefficient, S is the windward area of the abrasive, and t_{p0} indicates that the particle begins to accelerate at the moment, t_p is the iteration termination time, P is the liquid pressure, and x is the displacement.

The first item is the viscous resistance, the second item is the virtual mass force, the third item is the Basset force, the fourth item is the pressure gradient force, the fifth item is the Magnus force, and the sixth item is the Saffman force.

3. Acceleration Mechanism of the Abrasive in a High-Pressure Pipeline

3.1. Iterative Algorithms. In the premixed abrasive jet, the abrasive particles are fluidized in the high-pressure abrasive tank and passed from the control valve, through the mixing chamber, and into the main flow of the high-pressure pipeline. An interaction force is generated due to unequal flow rates of the abrasive particles and the high-pressure water. The abrasive particles are subjected to the first acceleration. At this point, the following assumptions are made:

- (1) The volume of the premixed abrasive jet studied in the paper is approximately 5%. Considering the very sparse, solid-liquid two-phase flow, the interaction force between the abrasive particles is neglected
- (2) The abrasive is a rigid sphere

Abrasives are mainly affected by viscous drag, virtual mass, and Basset forces in high-pressure pipelines. Therefore, the Euler form of the differential equation for the movement of abrasive particles in a high-pressure pipe is

$$\begin{aligned} \frac{4\pi}{3} r_p^3 \rho_p \frac{dV_p}{dt} = & C_D \frac{1}{2} \rho_f |V_f - V_p| (V_f - V_p) S \\ & + \frac{2}{3} \pi \cdot r_p^3 \rho_f \frac{d}{dt} (V_f - V_p) \\ & + K_B \sqrt{\pi \mu \rho_f} r_p^2 \int_{t_{p0}}^{t_p} \frac{1}{\sqrt{t_p - \tau}} \left(\frac{d}{dt} (V_f - V_p) \right) d\tau, \end{aligned} \quad (2)$$

where the i step is set and the speed of the abrasive is V_i .

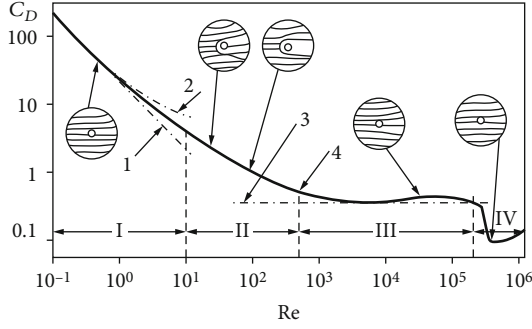


FIGURE 1: The relationship between the viscous resistance coefficient of the sphere and the Reynolds number. 1: Stokes' law; 2: Ossen's formula; 3: Newton's formula; 4: standard resistance curve.

The drag coefficient C_D is a key parameter in the calculation of resistance. The accuracy of this parameter directly affects the result of the resistance calculation. Since the boundary layer of the spherical particle surface is very complicated, there are only a few special cases where the C_D can be derived from the equations. At present, the drag coefficient is mainly determined experimentally. The relationship between the drag coefficient and the Reynolds number of a single rigid sphere, which was obtained by a large number of experiments in a stationary, isothermal, incompressible, and infinite flow field of fluid (referred to as the standard resistance curve), is shown in Figure 1.

Previous research often designated the drag coefficient as a constant or replaced it with a certain formula, which affected the calculation accuracy to some extent. To eliminate this effect, this study uses a real-time contrast interpolation method for analysis. The study utilizes MATLAB to identify the function depicted in Figure 1 and to establish a database of C_D values that change with the Reynolds number. The current Reynolds number is calculated according to the abrasive speed V_i and is compared to those in the database. Three sets of data are selected both before and after the current Reynolds number. According to the six sets of data and using the cubic spline interpolation method to find the resistance coefficient C_{Di} corresponding to the current Reynolds number, the viscous resistance can be expressed as

$$F_{di} = C_{Di} \frac{1}{2} \rho_f |V_f - V_{pi}| (V_f - V_{pi}) S. \quad (3)$$

The Basset force is a force related to the acceleration of abrasives. Let $t_{p0} = 0$, when calculating to the i th step, $t_{pi} = i \times \Delta t$, $\tau = n \times \Delta t$, then:

$$F_{Bi} = -K_B \sqrt{\pi \mu \rho_f} r_p^2 \times \sum_{n=1}^{i-1} \frac{1}{\sqrt{i \times \Delta t - n \times \Delta t}} \times a_i \times \Delta t. \quad (4)$$

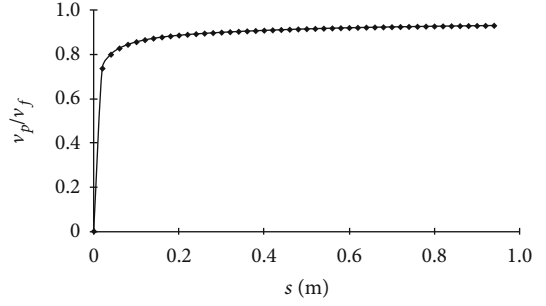


FIGURE 2: The distribution of velocity ratio of abrasive to water phase in the high-pressure pipe.

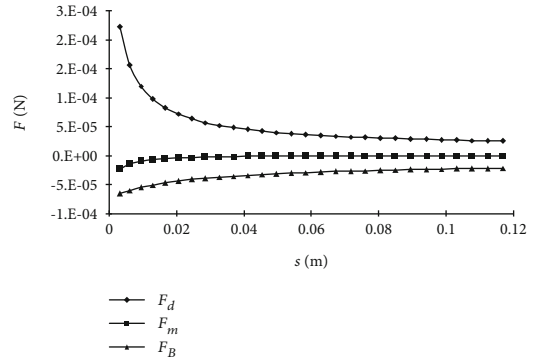


FIGURE 3: Abrasive stress distribution in the high-pressure pipe.

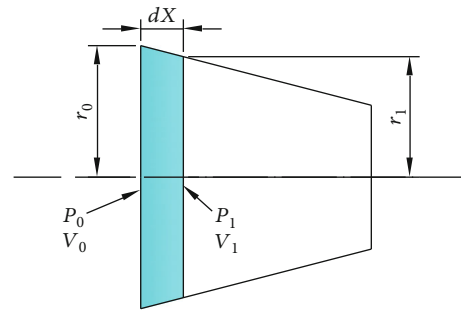


FIGURE 4: The sketch map of the pressure change in the nozzle's convergence section.

In the high-pressure pipeline, it can be assumed that the velocity V_f of the high-pressure water is constant, and the virtual mass force can be expressed as

$$F_{mi} = -\frac{2}{3} \pi \cdot r_p^3 \rho_f a_i. \quad (5)$$

For the simultaneous type 2 and the formula (5), the obtained acceleration expression is as follows:

$$a_i = \frac{F_{di} + F_{Bi}}{4/3\pi \cdot r_p^3 \rho_p + 2/3\pi \cdot r_p^3 \rho_f}. \quad (6)$$

The speed V_{i+1} and the displacement s_{i+1} of the abrasive at the $i+1$ th step are calculated according to the

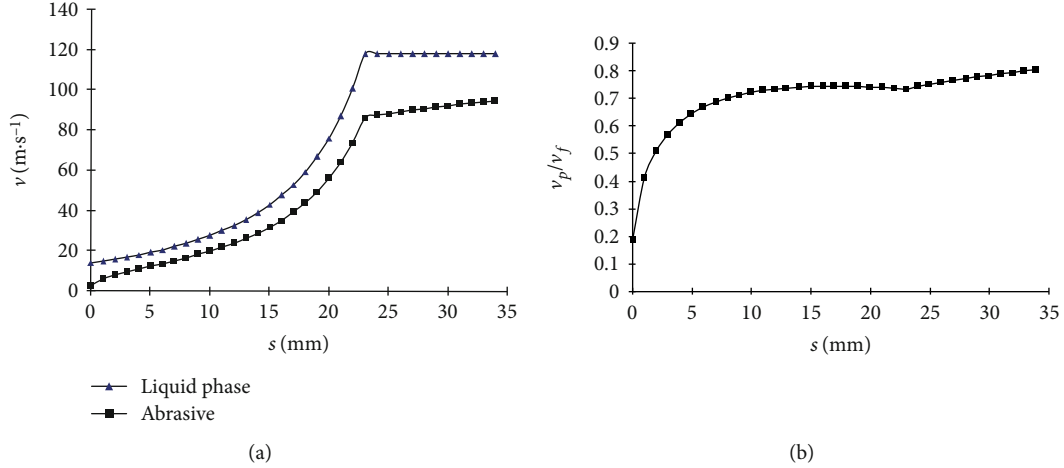


FIGURE 5: The velocity contrast curve of abrasive to water phase in the nozzle.

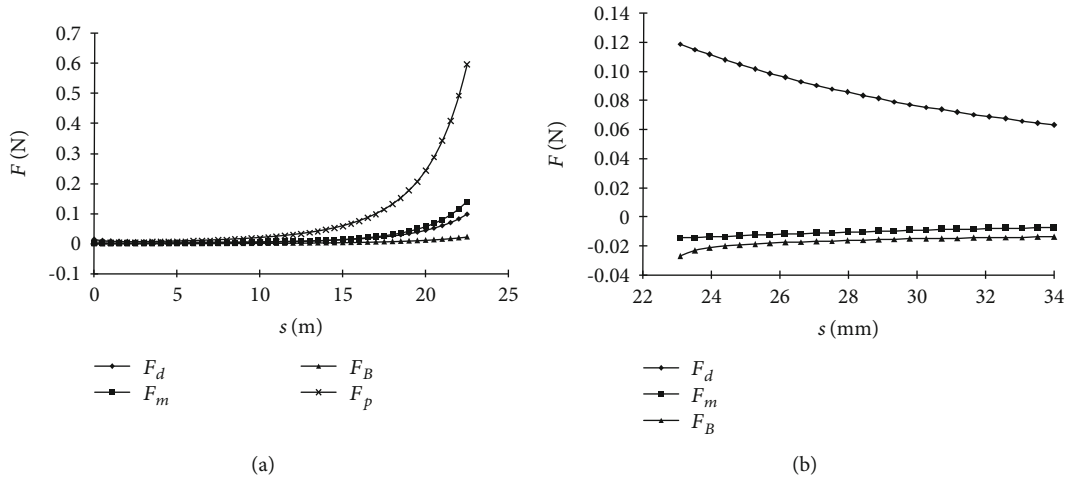


FIGURE 6: The stress distribution of abrasive in the nozzle.

acceleration, and the relevant parameters are brought into the iterative algorithm to continue the loop calculation.

3.2. Case Analysis. The high-pressure pipe in this study had a flow rate of 50 L/min and a diameter of 20 mm. The abrasive used was ceramsite, which has a size of 20 mesh, an abrasive apparent density of 2.7 kg/L, and a dynamic viscosity coefficient of $1.14 \times 10^{-3} \text{ kg}\cdot\text{m}^{-1}\cdot\text{s}^{-1}$. The time step was set at 0.00002 s, and the total step size was 20,000. The calculation result is shown in Figure 2.

It can be seen from Figure 2 that the abrasive accelerated to 0.2% of the liquid phase after 0.2 m of acceleration; after 0.8 m of acceleration, the speed had reached 92.6% of the liquid phase. The abrasive continued to accelerate until the speed was infinitely close to the speed of the liquid phase. Figure 3 shows the relationship between the forces and the displacement during the acceleration of the abrasive.

It can be seen from Figure 3 that the viscous resistance F_d coincides with the direction of the abrasive movement when the abrasive is accelerated in the pipeline and plays a major role in the acceleration of the abrasive. Depending on the mass force F_m and the Basset force F_B , the direction of the

abrasive movement is opposite, which acts to hinder the acceleration of the abrasive. During the acceleration of the abrasive, the virtual mass force F_m decays rapidly and gradually approaches zero. Although the viscous drag and the Basset are also attenuating, the decay rate is not fast. In the later stage of acceleration, the abrasive movement is mainly affected by viscous drag and Basset forces, but the two directions are opposite. As the difference between the abrasive accelerations gradually decreases, the abrasive acceleration also decays rapidly, but the speed of the abrasive and liquid phase at this point is infinitely close.

4. Acceleration Mechanism of the Abrasive in the Nozzle

The abrasive accelerated for the first time within the high-pressure pipeline; however, the kinetic energy obtained by the abrasive was small because of the small flow velocity in the pipeline. The second acceleration of the abrasive was accomplished in the nozzle. In this paper, the common conical convergent nozzle is taken as the research object.

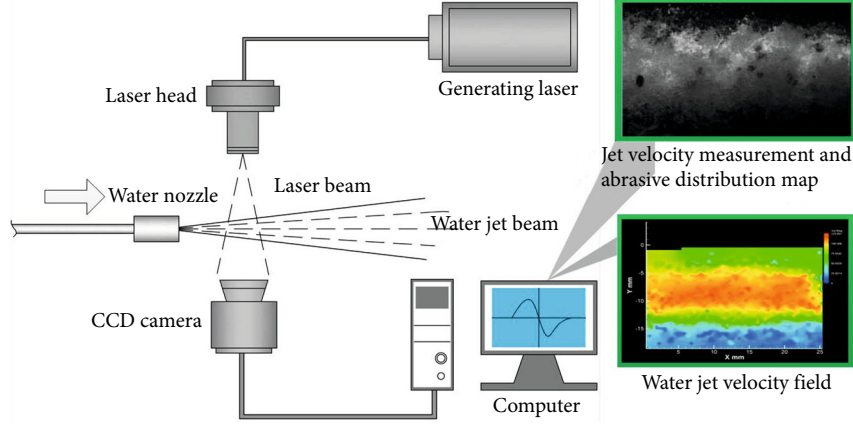


FIGURE 7: System diagram of velocity measurement with an abrasive jet.

4.1. Iterative Algorithm. The abrasive is mainly affected by viscous resistance, virtual mass force, and Basset force in the straight section of the nozzle. Its algorithm is consistent with that of abrasive in the pipeline, which is not discussed here. Abrasives are affected not only by the above three forces but also by the pressure gradient force in the convergence section of the nozzle. The Eulerian form of the differential equation for motion can be expressed as follows:

$$\begin{aligned}
 \frac{4\pi}{3}r_p^3\rho_p\frac{dV_p}{dt} &= C_D\frac{1}{2}\rho_f|V_f - V_p|(V_f - V_p)S \\
 &+ \frac{2}{3}\pi\cdot r_p^3\rho_f\frac{d}{dt}(V_f - V_p) \\
 &+ K_B\sqrt{\pi\mu\rho_f}r_p^2\int_{t_{p0}}^{t_p}\frac{1}{\sqrt{t_p - \tau}}\left(\frac{d}{dt}(V_f - V_p)\right) \\
 &\cdot d\tau - \left(\frac{4}{3}\pi r_p^3\right)\frac{\partial p}{\partial x}.
 \end{aligned} \tag{7}$$

In step 1, the velocity of the abrasive is V_i , and the calculation of viscous resistance, Basset force, and virtual mass force is as follows. Step 2 will not be repeated here. In this paper, the pressure gradient force was analyzed in detail. The pressure gradient force is a force formed by nonuniformity of the additional pressure distribution caused by the pressure gradient, which is the key parameter of the force. As shown in Figure 4, a schematic of the pressure change is given for displacement dx .

Assuming that water is incompressible and the change of gravitational potential energy of liquid phase in the nozzle can be neglected, it can be seen from the law of conservation of mass and Bernoulli equation:

$$P_0 - P_1 = \frac{1}{2}\rho_f V_0^2 \left(\frac{r_0}{r_1} - 1\right) \left(\frac{r_0}{r_1} + 1\right) \left[\left(\frac{r_0}{r_1}\right)^2 + 1\right]. \tag{8}$$

TABLE 1: Parameter settings for the experiment.

Type	Cylindrical
Nozzle length of straight segment (mm)	5, 7, 9, 11
Nozzle length of convergence section (mm)	14, 17, 20, 23
Nozzle inner diameter (mm)	3
Nozzle inlet flow (L/min)	50
Abrasive	Ceramsite
Abrasive mean diameter (mm)	0.425-0.85
Abrasive density (kg/m ³)	2.7

TABLE 2: The descriptive statistics of abrasive's velocity.

	Mean	Standard deviation	Standard error of mean
V (abrasive speed)	94.70	3.74	0.563

Since it is infinitesimal, formula (8) can be simplified to

$$P_0 - P_1 = \frac{\rho_f V_0^2 dx \tan(\theta/2)}{2r_0}. \tag{9}$$

Therefore, the pressure gradient force can be expressed as

$$F_{pi} = \frac{4}{3}\pi r_p^3 \frac{\rho_f V_{fi}^2 \tan(\theta/2)}{2r_{pi}}. \tag{10}$$

Then, the expression of acceleration is as follows:

$$a_i = \frac{F_{di} + F_{pi} + F_{Bi}}{\left(\frac{4}{3}\pi \cdot r_p^3 \rho_p + \frac{2}{3}\pi \cdot r_p^3 \rho_f\right)}. \tag{11}$$

According to the acceleration calculation, the velocity of the abrasive V_{i+1} and the displacement $s_i + 1$ are calculated at step $i + 1$. When the displacement $s_i + 1$ of the abrasive is larger than the length of the convergence section of the nozzle, the calculation stops. When the displacement $s_i + 1$ of the

TABLE 3: *T*-test of abrasive's velocity sample.

	<i>t</i>	df	Sig (bilateral)	Mean difference	Lower limit	Upper limit
V (abrasive speed)	0.352	46	0.726	0.198	93.19	96.21

abrasive is smaller than the length of the convergence section of the nozzle, the cycle calculation continues. When the abrasive accelerates in the straight section of the nozzle, the calculation is carried out according to the iteration algorithm in step 3. When the abrasive displacement is greater than the length of the straight section of the nozzle, the iteration ends.

4.2. Example Analysis. The conditions of the numerical example analysis are as follows: the flow rate is 50 L/min, the diameter of the high-pressure pipeline is 20 mm, the abrasive type is ceramsite, the abrasive size is 20 mesh, the apparent density of the abrasive is 2.7 kg/L, the dynamic viscous coefficient is $1.14 \times 10^{-3} \text{ kg m}^{-1} \text{ s}^{-1}$, the time step is 0.00002 s, the total step length is 20,000, the nozzle diameter is 3 mm, the convergence length is 23 mm, the linear segment length is 11 mm, and the convergence angle is 14 degrees. Assuming that the abrasive accelerates sufficiently in the high-pressure pipeline, the velocity of the liquid phase in the pipeline can be regarded as the initial velocity of the abrasive at the nozzle entrance. The above parameters are substituted into the iteration program for calculation, and the results are shown in Figure 5.

As seen from Figure 5(a), the liquid phase acceleration in the convergence zone is accompanied by a significant increase in the abrasive speed. In the first half of the convergence section of the nozzle, the liquid velocity is not substantial, and the abrasive velocity is not increasing rapidly. In the second half of the convergence stage, the liquid phase velocity increases sharply, and the abrasive velocity also increases sharply. From Figure 5(b), it can be seen that the velocity of the abrasive rapidly approaches that of the liquid phase when the displacement is less than 10 mm, indicating that the acceleration of abrasive is greater than that of the liquid phase. In the first half of the convergence stage, the change in the flow area is slow, the liquid phase acceleration is slow, and the initial abrasive velocity is low. There is a notable difference between the abrasive velocity and the liquid phase velocity, which suggests that the abrasive acceleration is greater than the liquid phase acceleration. In the second half of the convergence stage, the liquid velocity increases sharply and the abrasive acceleration delays, so the velocity ratio decreases after 15 mm. In the straight-line section, the liquid phase velocity remains unchanged, and the abrasive velocity at the nozzle outlet reaches 80% of the liquid phase. Thus, there is still a certain gap between the abrasive velocity and the liquid phase velocity. Figure 6 shows the relationship between forces and displacements in the process of abrasive acceleration.

Figure 6(a) shows that the pressure gradient force, virtual mass force, viscous drag force, and Basset force are applied to the abrasive in the convergence section of the nozzle from large to small. The pressure gradient force plays a particularly major role. Figure 6(b) shows that the force acting on the

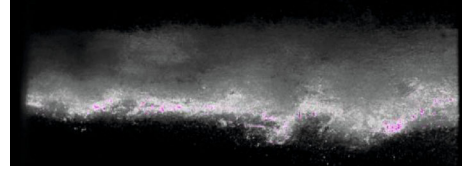


FIGURE 8: The pure water jet picture taken by PIV.

abrasive in the straight line of the nozzle is viscous resistance, Basset force, and virtual mass force, in turn. The viscous resistance is consistent with the direction of abrasive motion and plays a major role in the acceleration process. The virtual mass force and Basset force are opposite to the direction of acceleration, which hinders acceleration. Equation (7) shows that the viscous resistance is related to the velocity difference between the abrasive and the liquid phase, so the viscous resistance decreases with the acceleration of the abrasive. The virtual mass force and Basset force are related to the acceleration of the abrasive, while the acceleration of the abrasive in the straight section changes little; thus, the virtual mass force and Basset force change little. The summary analysis shows that the acceleration of abrasive is slow in the straight section of the nozzle.

5. Experimental Verification

5.1. Experimental Equipment and Methods. The models were assessed by comparing the calculated and experimental particle velocities measured using a particle image velocimetry (PIV) system. PIV is a nonintrusive laser-optical method for fast flow field measurement. In a PIV system, a laser generates a thin light sheet inside the flow. With a pulsed laser, a cross-correlation camera acquires two consecutive images of the particles transported with the flow. The particles have a displacement proportional to the flow velocity. With the known pulse distance and the calibrated scaling factor of the camera, the flow velocity can be calculated by the specialized software with the system. A detailed description of the PIV measurement technique can be found in one paper by Zuo et al. [19].

The PIV system used in this paper is produced by TSI Company. The specific information is as follows: (1) laser model: PIV00461, output energy: $2 \times 120 \text{ mJ/pulse}$; (2) light arm and light source lens group model: 610015-SOL; (3) synchronizer model: 610034; (4) CCD camera model: 630057, resolution: $1.6 \text{ K} \times 1.2 \text{ K}$, frame rate: 32 frames per second.

The abrasive speed test system diagram used in the experiment is shown in Figure 7. The system consists of two parts, a premixed abrasive generator and an abrasive speed tester.

The major parameter settings for the abrasive air jet are given in Table 1. The descriptive statistics of abrasive velocity are given in Table 2. The statistics of abrasive velocity at the nozzle exit can be seen in Table 3.

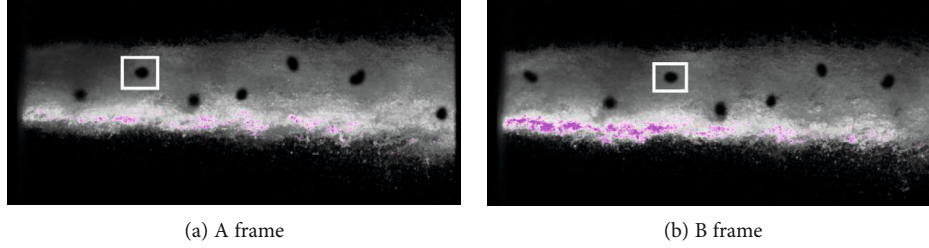


FIGURE 9: The picture of the abrasive water jet taken by PIV.

As shown in Figure 7, the jet is injected from left to right by nozzle 8, and the lamp light source 9 is irradiated from top to bottom. The irradiation surface is a vertical plane passing through the jet axis. The CCD camera is arranged perpendicular to the irradiation surface and photographs the irradiation surface from inside to outside. The range of the CCD camera is $19.94 \text{ mm} \times 14.85 \text{ mm}$, and the pixels are 1600×1192 . The size of each pixel is $12.46 \mu\text{m}$. The time interval between two photos in the same frame is $20 \mu\text{s}$. The obtained images are shown in Figures 8 and 9. The shooting range is 19.94 mm from the nozzle outlet to the target distance.

Figure 8 presents the results obtained for a pure water jet and Figure 9 for an abrasive jet. In Figures 9(a) and 9(b), the black spot circled by the white rectangle is the same abrasive, which clearly shows the direction of the abrasive movement. When the interval time between two pictures is known, the velocity of the abrasive can be obtained by calculating the displacement of the black spot.

5.2. Comparative Analysis. Four groups of nozzles with convergence section lengths of 23 mm , convergence angles of 14 degrees, and straight section lengths of 5 mm , 7 mm , 9 mm , and 11 mm were selected for experiments. The experimental flow rate was 50 L/min . PIV shooting conditions remain unchanged, with a shooting range from the nozzle outlet to the target distance of 19.94 mm and a shooting width of 14.85 mm . The Laida criterion was used to eliminate abnormal test data. The parameter hypothesis test was carried out for a nozzle with an 11 mm straight length. An abrasive theoretical velocity of 94.51 was the original hypothesis, while an alternative hypothesis of 94.5 was also considered. Given a significance level $= 0.01$, the test results returned by the statistical software SPSS are as follows:

Since the value $p = 0.726 \geq 0.01$ falls within the acceptance domain, the original hypothesis cannot be rejected; that is, there is no significant difference between the abrasive velocity parameter and the test value of 94.51 . Further, the 99% confidence interval tells us that there is a 99% chance that the abrasive velocity value is between $(93.19, 96.21)$, and 94.51 is included in this confidence interval, which also confirms the above inference; thus, the theoretical calculation and experimental results are satisfied.

Using the same method, based on the parameter hypothesis test, the abrasive velocity test results and theoretical values at the nozzle outlet with different linear lengths are verified, as shown in Table 4.

After the parameter hypothesis test, the experimental and theoretical values are compared and analyzed, and the results

TABLE 4: The statistics of abrasive's velocity at the exit of the nozzle.

Nozzle straight section length (mm)	Mean (m/s)	Standard deviation	Theoretical value (m/s)	Consistency
5	90.70	4.32	90.87	Satisfy
7	92.43	4.46	92.24	Satisfy
9	93.57	3.80	93.44	Satisfy
11	94.70	3.74	94.51	Satisfy

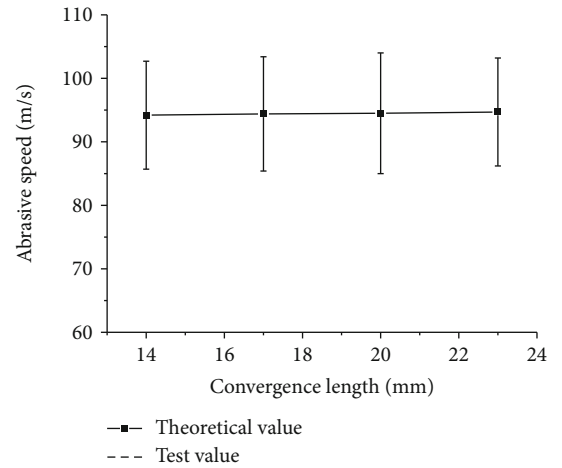


FIGURE 10: The velocity contrast figure of abrasive at the exit of the nozzle with different lengths of a straight segment.

show that the experimental and theoretical values meet the consistency. Figure 10 is a comparison between the theoretical and experimental results of abrasive velocity at the nozzle outlet.

From Figure 10, the theoretical value of abrasive velocity agrees well with the experimental value. The deviation between the theoretical value and the experimental mean value is 0.19 m/s , and the standard deviation is $3.74\text{--}4.46 \text{ m/s}$. The experimental results are in good agreement with the calculated results.

Four groups of nozzles with linear lengths of 11 mm , convergence angles of 14 degrees, and convergence section lengths of 14 mm , 17 mm , 20 mm , and 23 mm were selected for the same experiment. Using the Laida criterion to eliminate abnormal test data, the mean and standard deviation of the abrasive velocity at the nozzle outlet, with different lengths of convergence sections, were obtained and validated

TABLE 5: The statistics of abrasive's velocity at the exit of the nozzle.

Nozzle straight section length (mm)	Mean (m/s)	Standard deviation	Theoretical value (m/s)	Consistency
14	94.20	3.93	94.28	Satisfy
17	94.40	4.22	94.38	Satisfy
20	94.51	3.81	94.48	Satisfy
23	94.69	3.82	94.51	Satisfy

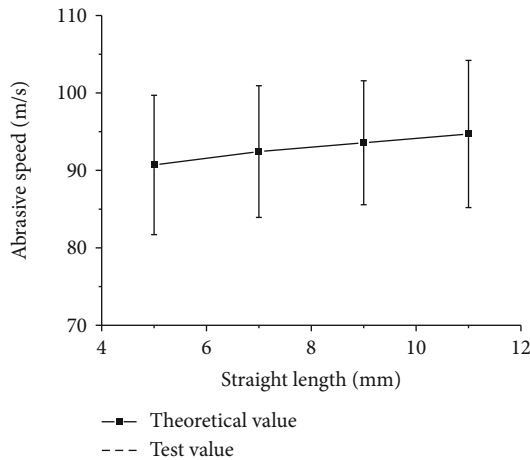


FIGURE 11: The velocity contrast figure of abrasive at the exit of the nozzle with different lengths of the convergence section.

by the parameter hypothesis test and theoretical value, as shown in Table 5.

After the parameter hypothesis test, the experimental and theoretical values were compared and analyzed, and the results show that the experimental and theoretical values are consistent. Figure 11 is a comparison between the theoretical and experimental results of abrasive velocity at the nozzle exit.

Figure 11 shows that the theoretical value of the abrasive velocity is in good agreement with the experimental value. The deviation between the theoretical value and the experimental mean is 0.18 m/s, and the standard deviation is 3.81–4.22 m/s. The experimental results are in good agreement with the revariation trend of the calculated results.

6. Conclusion

The theoretical analysis and corresponding mathematical model of the velocity of the premixed abrasive jet have been put forward. The real-time contrast interpolation method is utilized to solve the problem of the variable drag coefficient. In this paper, a numerical method is proposed to calculate the particle velocity, by discretizing the high-pressure pipe and nozzle into several small sections, along the axial direction. By comparing the calculated and measured particle velocity data, the model is verified experimentally. The results prove that the model prediction is in effective agreement with the experimental results, and the average error is less than 4%.

Nomenclature

V : Jet velocity
 C_D : Drag coefficient
 ρ : Liquid density
 t : Time
 τ : Duration of the peak pressure
 S : Windward area of abrasive.

Data Availability

As for the data availability statement, some or all data, models, or code generated or used during the study are available from the corresponding author by request (list items).

Conflicts of Interest

No conflict of interest exists in the submission of this manuscript.

Authors' Contributions

The manuscript is approved by all authors for publication.

Acknowledgments

This work is jointly supported by the National Natural Science Foundation of China (Nos. 51604092, 51774119, 51704096, and 51804115), the China Postdoctoral Science Foundation (No. 2018M642749) Key Scientific Research Project of Colleges and Universities in Henan Province (No. 21A44009), and the Natural Science Foundation of Henan Province (No. 182300410128). Zuo Weiqin received his B.S. and Ph.D. degrees from Chongqing University, China, in 2007 and 2012. He is now an associate professor at Henan Polytechnic University.

References

- [1] R. Melentiev and F. Fang, "Recent advances and challenges of abrasive jet machining," *CIRP Journal of Manufacturing Science and Technology*, vol. 22, pp. 1–20, 2018.
- [2] J. G. Kim and J. J. Song, "Abrasive water jet cutting methods for reducing blast-induced ground vibration in tunnel excavation," *International Journal of Rock Mechanics and Mining Sciences*, vol. 75, pp. 147–158, 2015.
- [3] Y. Xue, H. Si, D. Xu, and Z. Yang, "Experiments on the microscopic damage of coal induced by pure water jets and abrasive water jets," *Powder Technology*, vol. 332, pp. 139–149, 2018.
- [4] L. M. Hlaváč, I. M. Hlavacova, F. Arleo, F. Vigano, M. P. G. Annoni, and V. Geryk, "Shape distortion reduction method for abrasive water jet (AWJ) cutting," *Precision Engineering*, vol. 53, pp. 194–202, 2018.
- [5] R. S. Kumar, S. Gajendran, and R. Kesavan, "Estimation of optimal process parameters for abrasive water jet machining of marble using multi response techniques," *Materials Today: Proceedings*, vol. 5, no. 5, pp. 11208–11218, 2018.
- [6] Y. Liu, J. Zhang, J. Wei, and X. Liu, "Optimum structure of a Laval nozzle for an abrasive air jet based on nozzle pressure ratio," *Powder Technology*, vol. 364, no. 3, pp. 343–362, 2020.

- [7] F. L. Chen and E. Siores, "The effect of cutting jet variation on striation formation in abrasive water jet cutting," *International Journal of Machine Tools & Manufacture*, vol. 41, no. 10, pp. 1479–1486, 2001.
- [8] R. H. M. Jafar, H. Nouraei, M. Emamifar, M. Papini, and J. K. Spelt, "Erosion modeling in abrasive slurry jet micro-machining of brittle materials," *Journal of Manufacturing Processes*, vol. 17, pp. 127–140, 2015.
- [9] R. Laniel, O. Bouchareb, A. Brient, and M. Miroir, "Discrete elements model of an abrasive water-jet through the focal canon to the work-piece," *Procedia CIRP*, vol. 58, pp. 529–534, 2017.
- [10] F. Wang, R. Wang, W. Zhou, and G. Chen, "Numerical simulation and experimental verification of the rock damage field under particle water jet impacting," *International Journal of Impact Engineering*, vol. 102, pp. 169–179, 2017.
- [11] X. Liu, S. Liu, and H. Ji, "Numerical research on rock breaking performance of water jet based on SPH," *Powder Technology*, vol. 286, pp. 181–192, 2015.
- [12] A. N. J. Stevenson and I. M. Hutchings, "Scaling laws for particle velocity in the gas-blast erosion test," *Wear*, vol. 181–183, pp. 56–62, 1995.
- [13] F. Huang, S. Li, Y. Zhao, and Y. Liu, "Study on lateral jetting range during an arc-curved jet impacting nonplanar solid surfaces," *Journal of Fluids Engineering*, vol. 140, no. 10, article 101201, 2018.
- [14] F. Huang, S. Li, Y. Zhao, and Y. Liu, "A numerical study on the transient impulsive pressure of a water jet impacting nonplanar solid surfaces," *Journal of Mechanical Science and Technology*, vol. 32, no. 9, pp. 4209–4221, 2018.
- [15] R. K. Swanson, M. Kilman, and S. Cerwin, "Study of particle velocities in water driven abrasive jet cutting," in *Proceedings of the 4th US Water Jet Conference*, pp. 103–107, Berkeley, CA, USA, 1987.
- [16] A. L. Miller and J. H. Archibald, "Measurement of particle velocities in an abrasive jet cutting system," in *Proceedings from the 6th American Water Jet Conference*, pp. 291–304, Houston, TX, USA, 1991.
- [17] A. W. Momber and R. Kovacevic, "Energy dissipative processes in high speed water-solid particle erosion," in *Annual Meeting of American Society of Mechanical Engineers*, pp. 243–256, New York, NY, USA, 1995.
- [18] Y. J. Choo and C. H. Song, "PIV measurements of turbulent jet and pool mixing produced by a steam jet discharge in a sub-cooled water pool," *Nuclear Engineering and Design*, vol. 240, no. 9, pp. 2215–2224, 2010.
- [19] W. Zuo, X. Wang, F. Hao, Y. Lu, and M. Liu, "Research on acceleration mechanism of abrasive in pre-mixed abrasive water-jet based on iterative algorithm," *Journal of China University of Petroleum (Edition of Natural Science)*, vol. 40, no. 4, pp. 104–109, 2016.